CMS Physics Analysis Summary

Contact: cms-pag-conveners-heavyions@cern.ch 2013/05/07

Study of dijet momentum balance and pseudorapidity distributions in pPb collisions at $\sqrt{s_{\mathrm{NN}}} = 5.02$ TeV

The CMS Collaboration

Abstract

Results on dijet production in pPb collisions at a nucleon-nucleon center-of-mass energy of 5.02 TeV are presented. A data sample corresponding to an integrated luminosity of 18.48 nb^{-1} collected with the CMS detector at the LHC is analyzed. Jets are reconstructed with the anti-k_{T} algorithm, using combined information from tracking and calorimetry. The dijet momentum balance, azimuthal angle correlations and pseudorapidity distributions are studied as a function of forward calorimeter transverse energy and compared to results from PYTHIA reference calculations representing pp collisions. For pPb collisions, the dijet momentum ratio $p_{\mathrm{T},2}/p_{\mathrm{T},1}$ and the width of the azimuthal angle difference distribution is remarkably insensitive to the forward activity of the collision, and comparable to the same quantity obtained from the simulated pp reference. The pseudorapidity of the dijet system changes monotonically with increasing forward calorimeter activity in the direction expected from gluon saturation.

1 Introduction

High-energy collisions of heavy ions allow one to study the fundamental theory of the strong interaction – quantum chromodynamics (QCD) – in extreme conditions of temperature and energy density. Lattice QCD calculations [1] predict a new form of matter at energy densities above $\varepsilon_{\text{crit}} \approx 1$ GeV/fm^3 consisting of an extended volume of deconfined and chirally-symmetric (bare-mass) quarks and gluons: the Quark Gluon Plasma (QGP) [2–5]. One of the most interesting experimental signatures of QGP formation is "jet-quenching" due to in-medium energy loss when hard-scattered partons pass through the medium. Unbalanced back-to-back dijet correlations have long been proposed as a particularly useful tool for studying the QGP [6, 7]. In the first PbPb collisions at the LHC, the effects of this medium were observed in the early jet measurements [8–11].

Recent results at the LHC [8–14], using fully reconstructed jets, correlations between jets and single particles, and charged particle measurements, provide detailed information on the jet-quenching effect. For head-on collisions, a large broadening of the dijet momentum asymmetry distributions is observed, consistent with theoretical calculations that involve differential energy loss of back-to-back hard-scattered partons as they traverse the medium [15–17]. At leading order (LO) and in the absence of parton energy loss in the QGP, the two jets have equal transverse momenta (p_{T}) with respect to the beam axis and are completely correlated in the azimuthal angle ($\Delta\varphi_{1,2} = |\varphi_1 - \varphi_2| \approx \pi$). However, medium-induced gluon emission in the final state can significantly unbalance the energy between the two highest p_{T} (leading) jets, causing enhanced production of decorrelated dijets. This medium effect in nuclear interactions is expected to be much larger than that due to higher-order gluon radiation which is present for jet events even in pp collisions. Studies of dijet properties in pPb collisions are of great importance to establish a QCD baseline for hadronic interaction with cold nuclear matter [18, 19]. The dijet production rates as a function of jet pseudorapidity are also proposed to be a useful tool to probe the nuclear modifications of the parton distribution function.

In this paper, the first dijet momentum balance and pseudorapidity distribution measurements as a function of forward calorimeter activity are presented. These analyses use a large dataset of pPb collisions collected with the Compact Muon Solenoid (CMS) detector in 2013.

2 Experimental setup

This analysis uses a pPb data set corresponding to an integrated luminosity of $\int \mathcal{L}dt = 18.48\,\text{nb}^{-1}$ collected in early 2013. The center-of-mass energy per nucleon pair for the pPb collisions was $\sqrt{s_{NN}} = 5.02$ TeV, corresponding to beam energies of 4 TeV and 1.58 TeV (per nucleon) for protons and lead nuclei, respectively. As the nucleon-nucleon center-of-mass in these pPb collisions is not at rest in the laboratory frame, particles emitted at $\eta_{\text{cm}} = 0$ in the nucleon-nucleon center-of-mass frame will be detected at $\eta = -0.465$ in the laboratory frame since the higher energy proton beam traveled in the clockwise direction (i.e. $\theta = \pi$, where θ is the polar angle of the particle with respect to the anti-clockwise direction).

A detailed description of the CMS experiment can be found in Ref. [20]. The detector subsystem used for this analysis consists of the tracker, located in the 3.8 T magnetic field of the superconducting solenoid. It consists of 1440 silicon pixel and 15 148 silicon strip detector modules, with $\approx 10^7$ silicon strips, $\approx 6 \times 10^7$ pixels, and measures charged particles within the pseudorapidity range $|\eta| < 2.5$. It provides an impact parameter resolution of $\approx 15\,\mu$m and a transverse momentum (p_{T}) resolution of about 1.5% for 100 GeV/c particles. Also located inside the solenoid are the electromagnetic calorimeter (ECAL) and the hadron calorimeter (HCAL). The ECAL

consists of more than 75 000 lead-tungstate crystals, arranged in a quasi-projective geometry and distributed in a barrel region ($|\eta| < 1.48$) and two endcaps that extend up to $|\eta| = 3.0$. The HCAL barrel and endcaps are sampling calorimeters composed of brass and scintillator plates, covering $|\eta| < 3.0$. Iron forward calorimeters (HF) with quartz fibers, read out by photomultipliers, extend the calorimeter coverage up to $|\eta| = 5.0$ and are used to classify the pPb collisions. The detailed MC simulation of the CMS detector response is based on GEANT4 [21].

3 Event selection

The CMS online event selection employs a hardware-based level-1 trigger and a software-based high level trigger (HLT). The events used in this analysis were selected using an inclusive single-jet trigger in the HLT, requiring a calorimeter-based jet with corrected transverse momentum $p_{\mathrm{T}} > 100$ GeV/c. In additional to the jet data sample, a minimum bias event sample was triggered by requiring at least one track with $p_{\mathrm{T}} > 0.4$ GeV/c to be found in the pixel tracker for a pPb bunch crossing.

For the offline analysis, an additional selection of hadronic collisions was applied by requiring a coincidence of at least one HF calorimeter tower with more than 3 GeV of total energy on both the positive and negative sides of HF. Events with at least one reconstructed primary vertex with two or more associated tracks were selected with a maximum distance of the vertex to the nominal interaction point of 15 cm along the beam axis and less than 0.15 cm transverse distance to the beam trajectory. Events with a low fraction of good quality tracks originating from the primary vertex were rejected to suppress beam background [22]. The total number of selected events are corrected to a particle level selection, which is very similar to the actual selection described above: at least one particle (proper life time $\tau > 10^{-18}$ s) with $E > 3$ GeV in the pseudorapidity range $-5 < \eta < -3$ and one in the range $3 < \eta < 5$; this selection is referred to in the following as "double-sided" (DS) selection.

In addition to the event selection of inelastic hadronic collisions, the subsequent analysis requires a leading jet with corrected jet $p_{\mathrm{T},1} > 120$ GeV/c, a subleading jet in the event to have $p_{\mathrm{T},2} > 30$ GeV/c, and the azimuthal angle between the leading and subleading jet ($\Delta\phi_{1,2}$) to be larger than $2\pi/3$. Only offline reconstructed jets within $|\eta| < 3$ are considered in this analysis. No selection on the presence or absence of a third jet in the event is performed. In order to remove events with residual HCAL noise that are missed by the noise-rejection algorithms, either the leading or subleading jet is required to have at least one track of $p_{\mathrm{T}} > 4$ GeV/c. For all dijet observables, the subscripts 1 and 2 in the kinematical quantities always refer to the leading and subleading jets, respectively. For a data set of $\int \mathcal{L}dt = 18.48\,\mathrm{nb}^{-1}$, this selection yields 244,957 jet pairs.

The selected minimum bias and dijet events are divided into HF activity classes using the raw transverse energy measured by the HF detector in the pseudorapidity interval $|\eta| > 4$, denoted as $E_T^{HF[|\eta|>4]}$. Figure 1 shows the HF transverse energy distribution for the selected dijet events in comparison to that for minimum bias events. It can be seen that the selection of high-p_{T} dijet leads to a bias in the $E_T^{HF[|\eta|>4]}$ distributions toward higher value. The analysis is performed in five $E_T^{HF[|\eta|>4]}$ bins, 0–20, 20–25, 25–30, 30–40 and 40–100 GeV. The fractions of minimum bias events corrected to DS selection and dijet events passing the selection criteria above falling into each of the HF activity classes are provided in Table 1. By selecting on the same fraction of events in each sample using $E_T^{HF[|\eta|>4]}$, the corresponding distributions of number of participating nucleons (N_{part}) in the HIJING [23] (version 1.383) Monte Carlo simulations are compared to each as shown in Figure 2.

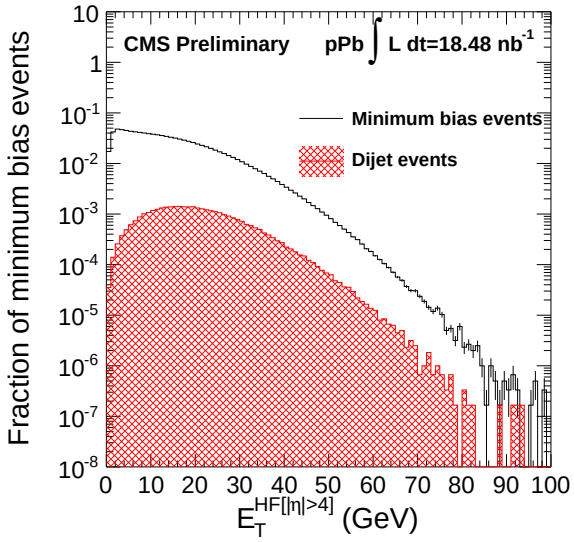

Figure 1: Probability distribution of the raw transverse energy measured by the HF detector in the pseudorapidity interval $|\eta| > 4$ for minimum bias collisions (black open histogram) and dijet events passing the dijet selection defined in this analysis (red hatched histogram).

Table 1: Fractions of the event sample for each HF activity class calculated for the DS selection and for the dijet selection. The last column shows the average multiplicity of reconstructed charged particles per bin with $|\eta| < 2.4$ and $p_{\mathrm{T}} > 0.4$ GeV/c ($N_{\mathrm{trk}}^{\mathrm{corrected}}$) after efficiency correction for DS events.

$E_T^{HF[\|\eta\|>4]}$ range (GeV)	Fraction of DS events	Fraction of dijet events	$\langle N_{\mathrm{trk}}^{\mathrm{corrected}} \rangle$ in DS events
0-20	73.1%	52.6%	33±2
20-25	10.5%	16.8%	74±3
25-30	7.1%	12.7%	88±4
30-40	6.8%	13.0%	106 ±5
40-100	2.5%	4.9%	135 ±6

4 Monte Carlo simulation

In order to study how the jet reconstruction is modified in pPb collisions, dijet events in pp collisions are simulated with the PYTHIA Monte Carlo generator (version 6.423, tune Z2) [24]. A minimum hard-interaction scale ($\hat{p}_{\mathrm{T}}$) selection of 30 GeV/c is used to increase the number of dijet events produced in the momentum range studied. To model the pPb underlying event, minimum bias pPb events are simulated with the HIJING event generator, version 1.383. The parameters of HIJING are tuned to reproduce the total particle multiplicities, charged hadron spectra, and to approximate the underlying event fluctuations seen in data.

The full detector simulation and analysis chain is used to process both PYTHIA dijet events and PYTHIA dijet events embedded into HIJING events (denoted PYTHIA+HIJING in this paper). The jet reconstruction is studied by using the PYTHIA generator jet information in comparison to the same fully reconstructed jet in PYTHIA+HIJING, matched in momentum space. The effects of the pPb underlying event on the jet position resolution, jet p_{T} scale, and jet-finding efficiency are studied as a function of HF transverse energy $E_T^{HF[|\eta|>4]}$, jet pseudorapidity and transverse momentum. These effects do not require corrections on the results but contribute to the systematic uncertainties.

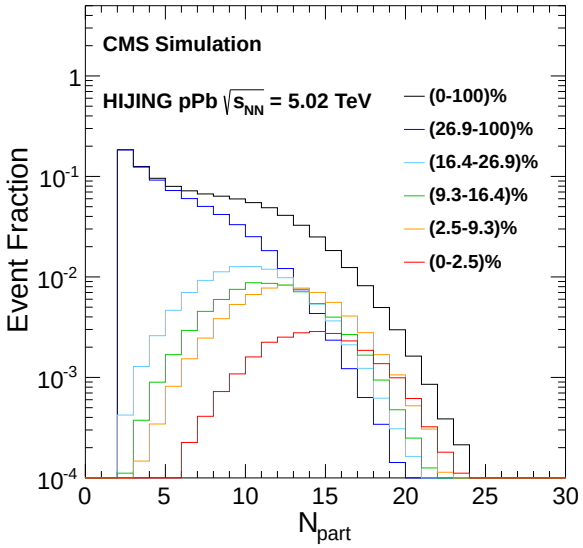

Figure 2: Probability distributions of number of participating nucleons (N_{part}) in the HIJING Monte Carlo simulations in the six different event fraction intervals.

5 Jet reconstruction

Offline jet reconstruction is performed using the CMS "particle-flow" algorithm [25]. By combining information from all sub-detector systems, the particle-flow algorithm attempts to identify all stable particles in an event, classifying them as electrons, muons, photons, charged and neutral hadrons. The particle-flow candidate objects are clustered into jets using the anti-k_{T} sequential recombination algorithm provided in the FASTJET framework [26]. Results are obtained using a distance parameter $R = 0.3$.

The subtraction of the underlying event (UE) background employs an iterative algorithm described in [27], using the same implementation as in the PbPb analysis [8]. The energy of the particle-flow candidates is mapped into projective towers with the same segmentation as the HCAL, and the mean and the dispersion of the energies detected in rings of constant η are subtracted from the jet energy. Jets reconstructed without UE subtraction are also used for systematic uncertainty estimation.

The jet energies are then corrected to final state particle jets using a factorized multi-step approach [28]. The jet energy corrections are derived using simulated PYTHIA events, as well as dijet and photon+jet collision events [28].

6 Results and discussion

This analysis aims to measure the dijet energy balance and azimuthal angle correlation in pPb collisions which are motivated by the observation of dijet energy imbalance in PbPb collisions [8]. The dijet pseudorapidity distributions in pPb collisions, which are sensitive to a possible modification of the nuclear parton distribution function (nPDF) with respect to that of nucleons, are also studied.

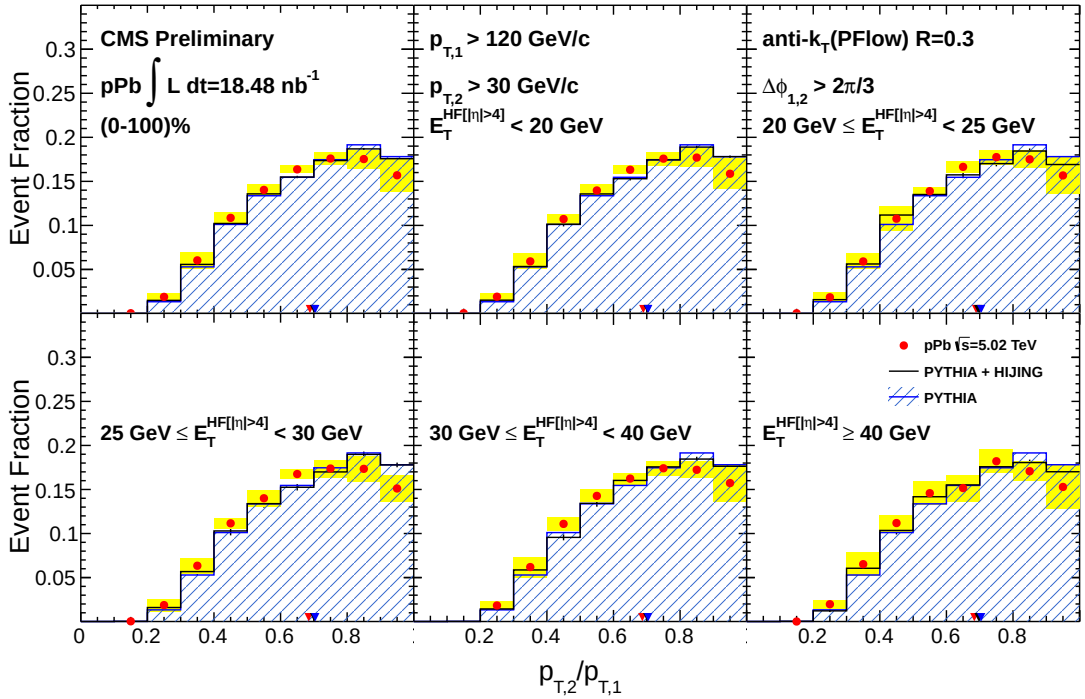

Figure 3: Dijet transverse momentum ratio ($p_{T,2}/p_{T,1}$) distributions for leading jets with $p_{T,1} > 120\,\text{GeV}/c$, subleading jets of $p_{T,2} > 30\,\text{GeV}/c$ and $\Delta\phi_{1,2} > 2\pi/3$. The first panel represents the minimum bias collisions without any selection on the HF transverse energy $E_T^{HF[|\eta|>4]}$, while the next five panels show the distributions in different $E_T^{HF[|\eta|>4]}$ classes. Results for pPb events are shown as red solid circles, while results for the simulated pp reference are shown as blue hatched histograms. The black histograms show the results for PYTHIA+HIJING simulated events. The arrows show the mean values of the distributions. The error bars represent the statistical uncertainties and the total systematic uncertainties are shown as yellow boxes.

6.1 Dijet momentum balance

As a function of collision centrality (i.e., the degree of overlap of the two colliding nuclei), dijet events in PbPb collisions were found to have an increasing momentum imbalance [8, 9, 11]. The same analysis is performed in pPb collisions. To characterize the dijet momentum balance (or imbalance) quantitatively, we use the dijet transverse momentum ratio $p_{T,2}/p_{T,1}$. As shown in Fig. 3, $p_{T,2}/p_{T,1}$ distributions measured in pPb data and PYTHIA agree within the systematic uncertainty in different $E_T^{HF[|\eta|>4]}$ intervals, including the event class with the largest forward calorimeter activity (0–2.5%). The residual difference in the dijet momentum ratio between data and PYTHIA+HIJING simulation is due to the slightly better jet energy resolution in MC simulation compared to data. In order to compare the dijet p_T ratio distribution to that in PbPb collisions, PbPb data collected at $\sqrt{s_{NN}} = 2.76$ TeV passing the same dijet selection are re-weighted to match the $E_T^{HF[|\eta|>4]}$ distributions measured in each HF activity class. Within the large statistical uncertainty in PbPb data, the dijet p_T ratio spectra in PbPb and pPb collisions are consistent with each other.

6.2 Dijet azimuthal correlations

Earlier studies of the dijet and photon-jet events in heavy-ion collisions [8–11] have shown very small modifications of dijet azimuthal correlations in PbPb collisions despite the large changes

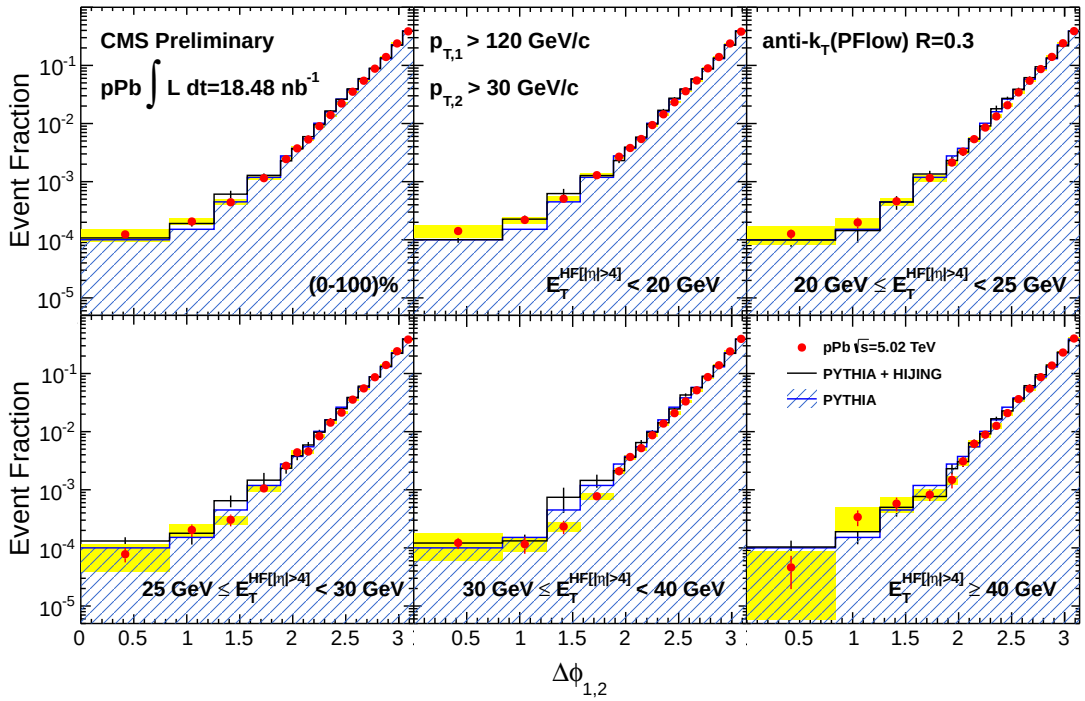

Figure 4: Distribution of the azimuthal angle $\Delta\phi_{1,2}$ between the leading and subleading jets for leading jets with $p_{T,1} > 120\,\mathrm{GeV}/c$ and subleading jets of $p_{T,2} > 30\,\mathrm{GeV}/c$. The first panel represents the minimum bias collisions without any selection on the HF transverse energy $E_T^{HF[|\eta|>4]}$, while the next five panels show the distributions in different $E_T^{HF[|\eta|>4]}$ classes. Results for pPb events are shown as red solid circles, while results for the simulated pp reference are shown as blue hatched histograms. The black histograms show the results for PYTHIA+HIJING simulated events. The error bars represent the statistical uncertainties and the total systematic uncertainties are shown as yellow boxes.

seen in the dijet momentum balance. This is an important aspect of the interpretation of energy loss observations [29].

Figure 4 shows the distributions of the azimuthal angle $\Delta\phi_{1,2}$ between the leading and subleading jets which pass the respective p_T selections in six HF activity classes, compared to PYTHIA and PYTHIA+HIJING simulation. The distributions from pPb data are in good agreement with the PYTHIA reference. To study the evolution of the shape, the distributions are fitted to a normalized exponential function:

$$\frac{1}{N_{\mathrm{dijet}}}\frac{dN_{\mathrm{dijet}}}{d\Delta\phi_{1,2}} = \frac{e^{(\Delta\phi-\pi)/\sigma}}{(1-e^{-\pi/\sigma})\,\sigma}. \tag{1}$$

The fit is restricted to the exponentially falling region $\Delta\phi_{1,2} > 2\pi/3$. The results of this fit for pPb data are summarized in Fig. 7. The fitted width of the azimuthal angle difference distribution does not vary as a function of $E_T^{HF[|\eta|>4]}$ and it is slightly narrower than in the PYTHIA simulation.

6.3 Dijet pseudorapidity

The dijet pseudorapidity distributions η_{dijet}, defined as $(\eta_1 + \eta_2)/2$, are studied in bins of $E_T^{HF[|\eta|>4]}$. Those distributions may reveal possible modifications of the nPDF with respect to that of nucleons. Depletion of low x partons in the lead ion may lead to a shift in the dijet pseudorapidity distribution toward the direction of the Pb beam. In this analysis, the dijet pseudorapidity is calculated in the laboratory frame. Due to the limited acceptance (jet $|\eta| < 3$) as well as the asymmetric pPb collision, where the lead ion is going in the positive z direction, the mean of the unmodified dijet pseudorapidity distribution will be at $\eta = -0.39$.

Figure 5 show the η_{dijet} distributions in different HF activity classes. The pPb data are compared to and PYTHIA+HIJING simulation. Modifications of the η_{dijet} distributions are observed with respect to the MC references. Figure 6 shows the comparison of the pPb data in different HF activity classes. As shown in the left panel of the Figure 6, a systematic and monotonic increase of the average η as a function of the HF transverse energy $E_T^{HF[|\eta|>4]}$ is observed. This is consistent with that as the HF transverse energy $E_T^{HF[|\eta|>4]}$ becomes larger, the mean longitudinal momentum carried by the partons in the lead ion increases, and thus has an observable influence on the pseudorapidity of the resulting dijet system. In order to compare the shape of the η_{dijet} distributions in the interval $\eta_{\text{dijet}} > 0$, the spectra from pPb data are normalized by the numbers of dijet events with $\eta_{\text{dijet}} > 0$ in the corresponding HF activity class. The shapes of the η_{dijet} in the region $\eta_{\text{dijet}} > 0$ are similar as shown in the right panel of the Figure 6.

7 Summary

Figure 7 summarizes the results obtained with pPb collisions. We observe a nearly constant $\sigma(\Delta\phi_{1,2})$ and transverse energy ratio of the dijets as a function of $E_T^{HF[|\eta|>4]}$. In addition, the lower panels show the mean and width of the dijet pseudorapidity distribution, measured using jets in the pseudorapidity interval $|\eta| < 3$ in the lab frame, as a function of the HF transverse energy, respectively. Those quantities change significantly with increasing forward calorimeter transverse energy, while the simulated pp dijets embedded in HIJING MC, representing pPb collisions, show no noticeable changes. A similar trend in dijet pseudorapidity is observed if the analysis is done in bins of HF transverse energy measured in either $\eta > 4$ or in $\eta < -4$.

In summary, the CMS detector has been used to study jet production in pPb collisions at $\sqrt{s_{NN}} = 5.02$ TeV. The anti-k_T algorithm is used to reconstruct jets based on combined tracker and calorimeter information. Events containing a leading jet with $p_{T,1} > 120$ GeV/c and a subleading jet with $p_{T,2} > 30$ GeV/c in the pseudorapidity range $|\eta| < 3$ are analyzed. Data are compared to PYTHIA as well as PYTHIA+HIJING dijet simulations, which are tuned to reproduce the observed underlying event fluctuations. Across the full range of forward calorimeter transverse energy, no significant dijet momentum imbalance or broadening of the dijet angular correlations is observed in the data with respect to the reference distributions. However, as a function of forward calorimeter transverse energy, a strong modification of the dijet pseudorapidity distribution is observed.

The results presented in this paper confirm that the observed dijet asymmetry in PbPb collisions is not originating from initial state effects. Modifications of the dijet pseudorapidity distribution with respect to the simulated pp reference is observed and the mean of the distribution changes monotonically with increasing forward calorimeter activity. These measurements provides quantitative constraints on the nPDF [30–34].

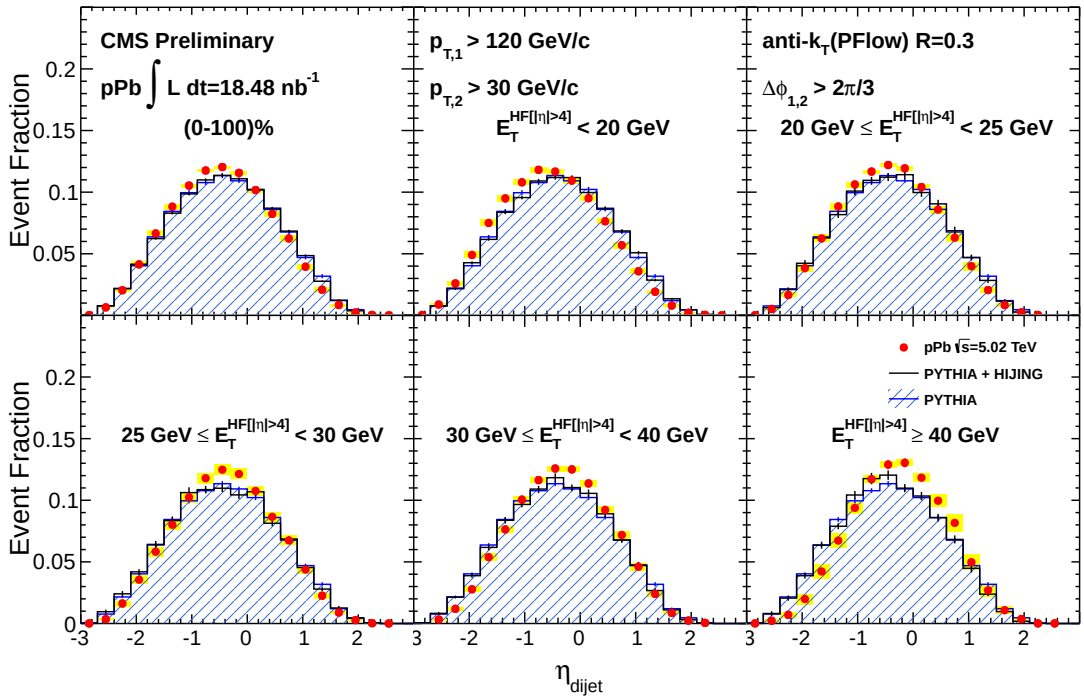

Figure 5: Distributions of dijet pseudorapidity (η_{dijet}) defined as $(\eta_1 + \eta_2)/2$ for leading jets with $p_{\mathrm{T},1} > 120\,\mathrm{GeV}/c$, subleading jets of $p_{\mathrm{T},2} > 30\,\mathrm{GeV}/c$ and $\Delta\phi_{1,2} > 2\pi/3$. The first panel represents the minimum bias collisions without any selection on the HF transverse energy $E_T^{HF[|\eta|>4]}$, while the next five panels show the distributions in different $E_T^{HF[|\eta|>4]}$ classes. Results for pPb events are shown as red solid circles, while results for the simulated pp reference are shown as blue hatched histograms. The black histograms show the results for PYTHIA+HIJING simulated events. The arrows show the mean values of the distributions. The error bars represent the statistical uncertainties and the total systematic uncertainties are shown as yellow boxes.

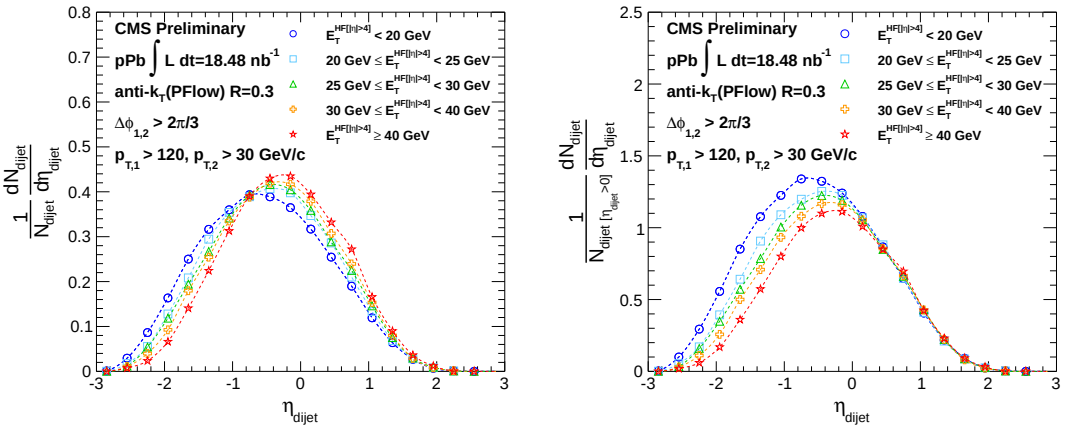

Figure 6: Dijet pseudorapidity distributions in the 5 HF activity classes. (Left panel) The distributions are normalized by the number of selected dijet events. (Right panel) The distributions are normalized by the number of dijet events with $\eta_{\mathrm{dijet}} > 0$.

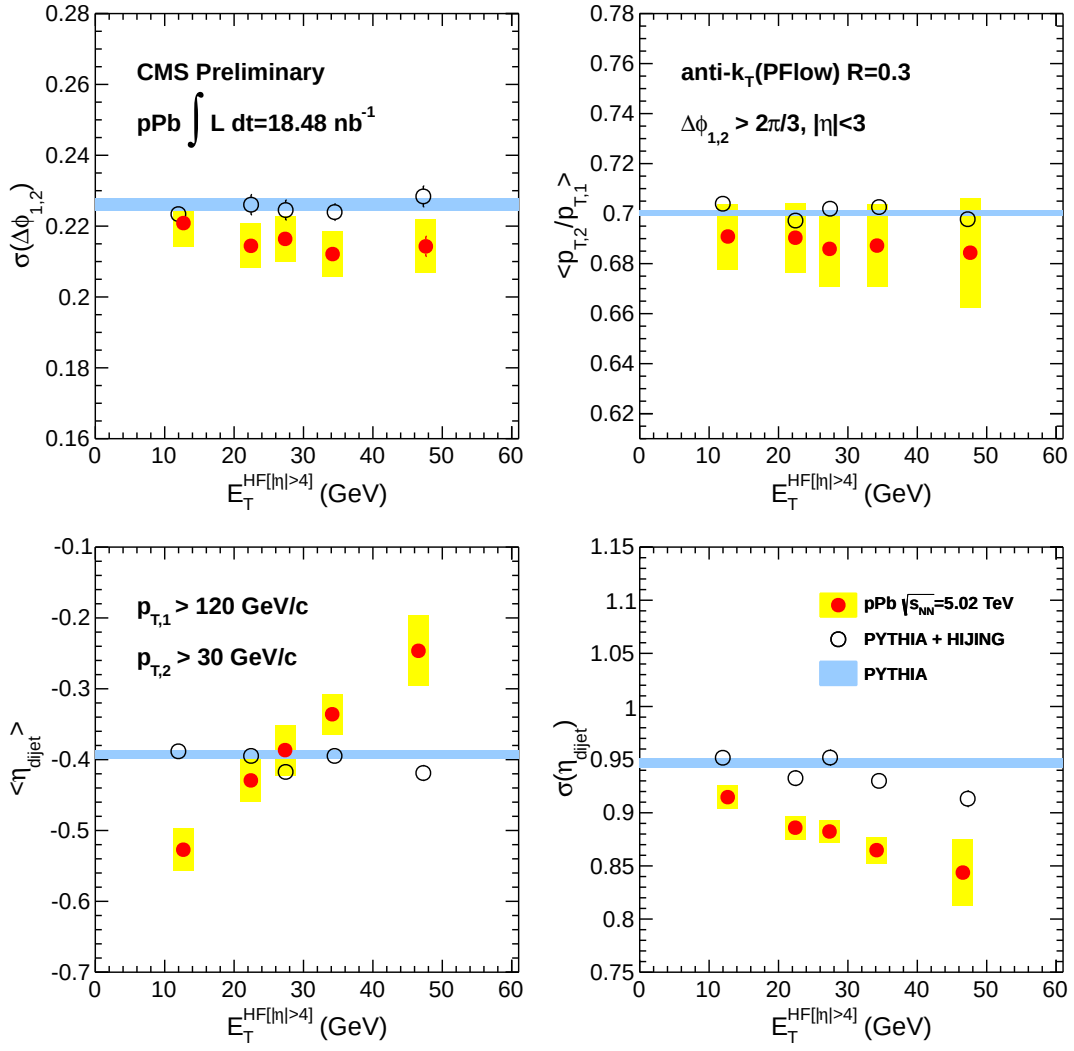

Figure 7: Summary of the dijet measurements as a function of $E_T^{HF[|\eta|>4]}$. (Upper left panel) Fitted $\Delta\phi_{1,2}$ width (σ in Eq. 1). (Upper right panel) Average ratio of dijet transverse momentum. (Lower left panel) Mean of η_{dijet} distribution. (Lower right panel) Standard deviation of η_{dijet} distribution. All panels show pPb data (red solid circles) compared to the PYTHIA+HIJING MC simulation (black open circles) and PYTHIA (blue band, where the band width indicate statistical uncertainty). The yellow boxes indicate the systematic uncertainties and the error bars denote the statistical uncertainties.

References

[1] F. Karsch and E. Laermann, "Thermodynamics and in-medium hadron properties from lattice QCD", in *Quark-Gluon Plasma III, R. Hwa (ed.)*, pp. 1–59. Hackensack, USA, 2003. arXiv:hep-lat/0305025.

[2] E. V. Shuryak, "Theory of Hadronic Plasma", *Sov. Phys. JETP* **47** (1978) 212.

[3] J. C. Collins and M. J. Perry, "Superdense Matter: Neutrons Or Asymptotically Free Quarks?", *Phys. Rev. Lett.* **34** (1975) 1353, doi:10.1103/PhysRevLett.34.1353.

[4] N. Cabibbo and G. Parisi, "Exponential Hadronic Spectrum and Quark Liberation", *Phys. Lett.* **B59** (1975) 67, doi:10.1016/0370-2693(75)90158-6.

[5] B. A. Freedman and L. D. McLerran, "Fermions and Gauge Vector Mesons at Finite Temperature and Density. 3. The Ground State Energy of a Relativistic Quark Gas", *Phys. Rev.* **D16** (1977) 1169, doi:10.1103/PhysRevD.16.1169.

[6] D. A. Appel, "Jets as a probe of quark-gluon plasmas", *Phys. Rev.* **D33** (1986) 717, doi:10.1103/PhysRevD.33.717.

[7] J. P. Blaizot and L. D. McLerran, "Jets in Expanding Quark - Gluon Plasmas", *Phys. Rev.* **D34** (1986) 2739, doi:10.1103/PhysRevD.34.2739.

[8] CMS Collaboration, "Observation and studies of jet quenching in PbPb collisions at nucleon-nucleon center-of-mass energy = 2.76 TeV", *Phys.Rev.* **C84** (2011) 024906, doi:10.1103/PhysRevC.84.024906, arXiv:1102.1957.

[9] CMS Collaboration, "Jet momentum dependence of jet quenching in PbPb collisions at $\sqrt{s_{NN}} = 2.76$ TeV", *Phys.Lett.* **B712** (2012) 176–197, doi:10.1016/j.physletb.2012.04.058, arXiv:1202.5022.

[10] CMS Collaboration, "Studies of jet quenching using isolated-photon+jet correlations in PbPb and pp collisions at $\sqrt{s_{NN}} = 2.76$ TeV", *Phys.Lett.* **B718** (2013) 773–794, doi:10.1016/j.physletb.2012.11.003, arXiv:1205.0206.

[11] ATLAS Collaboration, "Observation of a Centrality-Dependent Dijet Asymmetry in Lead-Lead Collisions at sqrt(S(NN))= 2.76 TeV with the ATLAS Detector at the LHC", *Phys.Rev.Lett.* **105** (2010) 252303, arXiv:1011.6182.

[12] ALICE Collaboration, "Particle-yield modification in jet-like azimuthal di-hadron correlations in Pb-Pb collisions at $\sqrt{s_{NN}} = 2.76$ TeV", *Phys.Rev.Lett.* **108** (2012) 092301, doi:10.1103/PhysRevLett.108.092301, arXiv:1110.0121.

[13] CMS Collaboration, "Study of high-pT charged particle suppression in PbPb compared to pp collisions at $\sqrt{s_{NN}} = 2.76$ TeV", *Eur.Phys.J.* **C72** (2012) 1945, doi:10.1140/epjc/s10052-012-1945-x, arXiv:1202.2554.

[14] ALICE Collaboration, "Suppression of Charged Particle Production at Large Transverse Momentum in Central Pb–Pb Collisions at $\sqrt{s_{NN}} = 2.76$ TeV", *Phys.Lett.* **B696** (2011) 30–39, doi:10.1016/j.physletb.2010.12.020, arXiv:1012.1004.

[15] Y. He, I. Vitev, and B.-W. Zhang, "$\mathcal{O}(\alpha_s^3)$ Analysis of Inclusive Jet and di-Jet Production in Heavy Ion Reactions at the Large Hadron Collider", *Phys.Lett.* **B713** (2012) 224–232, doi:10.1016/j.physletb.2012.05.054, arXiv:1105.2566.

[16] C. Young et al., "Dijet asymmetry at the energies available at the CERN Large Hadron Collider", *Phys.Rev.* **C84** (2011) 024907, doi:10.1103/PhysRevC.84.024907, arXiv:1103.5769.

[17] G.-Y. Qin and B. Muller, "Explanation of Di-jet asymmetry in Pb+Pb collisions at the Large Hadron Collider", *Phys.Rev.Lett.* **106** (2011) 162302, doi:10.1103/PhysRevLett.108.189904,10.1103/PhysRevLett.106.162302, arXiv:1012.5280.

[18] C. Salgado et al., "Proton-Nucleus Collisions at the LHC: Scientific Opportunities and Requirements", *J.Phys.* **G39** (2012) 015010, doi:10.1088/0954-3899/39/1/015010, arXiv:1105.3919.

[19] J. Albacete et al., "Predictions for p+Pb Collisions at $\sqrt{s_{NN}} = 5$ TeV", arXiv:1301.3395.

[20] CMS Collaboration, "The CMS experiment at the CERN LHC", *JINST* **3** (2008) S08004, doi:10.1088/1748-0221/3/08/S08004.

[21] GEANT4 Collaboration, "GEANT4: A simulation toolkit", *Nucl. Instrum. Meth.* **A506** (2003) 250, doi:10.1016/S0168-9002(03)01368-8.

[22] CMS Collaboration, "CMS Tracking Performance Results from early LHC Operation", *Eur.Phys.J.* **C70** (2010) 1165–1192, doi:10.1140/epjc/s10052-010-1491-3, arXiv:1007.1988.

[23] M. Gyulassy and X.-N. Wang, "HIJING 1.0: A Monte Carlo program for parton and particle production in high-energy hadronic and nuclear collisions", *Comput.Phys.Commun.* **83** (1994) 307, doi:10.1016/0010-4655(94)90057-4, arXiv:nucl-th/9502021.

[24] R. Field, "Early LHC Underlying Event Data - Findings and Surprises", arXiv:1010.3558.

[25] CMS Collaboration, "Commissioning of the Particle-Flow Reconstruction in Minimum-Bias and Jet Events from pp Collisions at 7 TeV", *CMS Physics Analysis Summary* **CMS-PAS-PFT-10-002** (2010).

[26] M. Cacciari, G. P. Salam, and G. Soyez, "The Anti-k(t) jet clustering algorithm", *JHEP* **0804** (2008) 063, doi:10.1088/1126-6708/2008/04/063, arXiv:0802.1189.

[27] O. Kodolova et al., "The performance of the jet identification and reconstruction in heavy ions collisions with CMS detector", *Eur. Phys. J.* **C50** (2007) 117, doi:10.1140/epjc/s10052-007-0223-9.

[28] CMS Collaboration, "Determination of Jet Energy Calibration and Transverse Momentum Resolution in CMS", *JINST* **6** (2011) P11002, doi:10.1088/1748-0221/6/11/P11002, arXiv:1107.4277.

[29] J. Casalderrey-Solana, J. Milhano, and U. Wiedemann, "Jet quenching via jet collimation", *J.Phys.* **G38** (2011) 124086, doi:10.1088/0954-3899/38/12/124086, arXiv:1107.1964.

[30] K. Eskola, V. Kolhinen, and P. Ruuskanen, "Scale evolution of nuclear parton distributions", *Nucl.Phys.* **B535** (1998) 351–371, doi:10.1016/S0550-3213(98)00589-6, arXiv:hep-ph/9802350.

[31] K. Eskola, H. Paukkunen, and C. Salgado, "EPS09: A New Generation of NLO and LO Nuclear Parton Distribution Functions", *JHEP* **0904** (2009) 065, doi:10.1088/1126-6708/2009/04/065, arXiv:0902.4154.

[32] M. Hirai, S. Kumano, and T.-H. Nagai, "Nuclear parton distribution functions and their uncertainties", *Phys.Rev.* **C70** (2004) 044905, doi:10.1103/PhysRevC.70.044905, arXiv:hep-ph/0404093.

[33] I. Schienbein et al., "PDF Nuclear Corrections for Charged and Neutral Current Processes", *Phys.Rev.* **D80** (2009) 094004, doi:10.1103/PhysRevD.80.094004, arXiv:0907.2357.

[34] D. de Florian and R. Sassot, "Nuclear parton distributions at next-to-leading order", *Phys.Rev.* **D69** (2004) 074028, doi:10.1103/PhysRevD.69.074028, arXiv:hep-ph/0311227.